Mapping the U.S. West Coast surface circulation: A multiyear analysis of high-frequency radar observations

Sung Yong Kim,[1] Eric J. Terrill,[1] Bruce D. Cornuelle,[1] Burt Jones,[2] Libe Washburn,[3] Mark A. Moline,[4] Jeffrey D. Paduan,[5] Newell Garfield,[6] John L. Largier,[7] Greg Crawford,[8,9] and P. Michael Kosro[10]

Received 21 September 2010; revised 22 November 2010; accepted 8 December 2010; published 5 March 2011.

[1] The nearly completed U.S. West Coast (USWC) high-frequency radar (HFR) network provides an unprecedented capability to monitor and understand coastal ocean dynamics and phenomenology through hourly surface current measurements at up to 1 km resolution. The dynamics of the surface currents off the USWC are governed by tides, winds, Coriolis force, low-frequency pressure gradients (less than 0.4 cycles per day (cpd)), and nonlinear interactions of those forces. Alongshore surface currents show poleward propagating signals with phase speeds of $O(10)$ and $O(100$ to $300)$ km day^{-1} and time scales of 2 to 3 weeks. The signals with slow phase speed are only observed in southern California. It is hypothesized that they are scattered and reflected by shoreline curvature and bathymetry change and do not penetrate north of Point Conception. The seasonal transition of alongshore surface circulation forced by upwelling-favorable winds and their relaxation is captured in fine detail. Submesoscale eddies, identified using flow geometry, have Rossby numbers of 0.1 to 3, diameters in the range of 10 to 60 km, and persistence for 2 to 12 days. The HFR surface currents resolve coastal surface ocean variability continuously across scales from submesoscale to mesoscale ($O(1)$ km to $O(1000)$ km). Their spectra decay with k^{-2} at high wave number (less than 100 km) in agreement with theoretical submesoscale spectra below the observational limits of present-day satellite altimeters.

Citation: Kim, S. Y., et al. (2011), Mapping the U.S. West Coast surface circulation: A multiyear analysis of high-frequency radar observations, *J. Geophys. Res.*, *116*, C03011, doi:10.1029/2010JC006669.

1. Introduction

[2] The use of shore-based high-frequency radar (HFR) to measure currents and waves at the ocean surface using Bragg scatter return from transmitted radio signals has a rich history with the remote sensing community and has developed into an oceanographic observational tool [e.g., *Crombie*, 1955; *Stewart and Joy*, 1974; *Barrick et al.*, 1977]. Operational systems provide hourly surface current fields in the upper $O(1)$ m depth with 0.5 to 6 km horizontal resolution extending from the nearcoast, excluding the surfzone, offshore to distances of 50 to 150 km depending on choice of radio frequency. Use of HFR for oceanographic research of ocean currents is a rapidly maturing field. Planning efforts are underway to instrument the entire U.S. coastline to provide a national capability to monitor and observe surface currents in real time. This network will support both scientific studies and operational needs, including connectivity studies, for monitoring and understanding marine protected areas and larval transport; the tracking of shoreline discharges, impaired water quality and spilled oil; and at-sea search and rescue efforts [e.g., *Ocean US*, 2002; *Ullman et al.*, 2006; Kaplan and Largier, 2006; *Kim et al.*, 2009b].

[3] Numerous observational efforts in the California Current on the U.S. West Coast (USWC) have identified and described physical phenomena with various scales. As one of the major subtropical eastern boundary currents extending from Vancouver Island to Baja California, the equatorward California Current in the oceanic offshore

[1]Scripps Institution of Oceanography, University of California, San Diego, La Jolla, California, USA.
[2]Department of Biological Sciences, University of Southern California, Los Angeles, California, USA.
[3]Institute for Computational Earth System Science, Department of Geography, University of California, Santa Barbara, California, USA.
[4]Biological Sciences Department, California Polytechnic State University, San Luis Obispo, California, USA.
[5]Department of Oceanography, Graduate School of Engineering and Applied Sciences, Naval Postgraduate School, Monterey, California, USA.
[6]Geosciences Department and Romberg Tiburon Center for Environmental Studies, San Francisco State University, Tiburon, California, USA.
[7]Bodega Marine Laboratory, University of California, Davis, Bodega Bay, California, USA.
[8]Department of Oceanography, Humboldt State University, Arcata, California, USA.
[9]Now at the Faculty of Science and Technology, Vancouver Island University, Nanaimo, British Columbia, Canada.
[10]College of Oceanic and Atmospheric Sciences, Oregon State University, Corvallis, Oregon, USA.

0148-0227/11/2010JC006669

regime and the strongly variable currents in the coastal regime have been observed, together with their persistent circulation patterns. The seasonal California Current is characterized by spring upwelling and fall relaxation over the continental shelf associated with seasonal wind forcing [e.g., *Strub et al.*, 1987; *Largier et al.*, 1993; *Strub and James*, 2000]. In the transition zone which divides the oceanic offshore regime and the coastal regime, instability of the shear flow and horizontal density gradients give rise to turbulent features including fronts, jets, and submesoscale eddies [e.g., *McWilliams*, 1985; *Capet et al.*, 2008]. Poleward propagating events have often been interpreted in the dynamical framework of coastally trapped waves (CTWs) [e.g., *Chapman*, 1987; *Brink*, 1991; *Ramp et al.*, 1997]. Moreover, barotropic and baroclinic tidal currents (herein called tide coherent currents) over the continental shelf and break regions have been observed [e.g., *Erofeeva et al.*, 2003; *Kaplan et al.*, 2005; *Rosenfeld et al.*, 2009].

[4] Although the physics, chemistry and biology of the California Current System (CCS) have been covered in many previous studies (e.g., ongoing California Cooperative Fisheries Investigation (CalCOFI) dates to 1949), this current system remains an active area of integrated monitoring and interdisciplinary research due to the importance of the ecosystem for USWC fisheries (e.g., California Current Large Marine Ecosystem (CCLME)) [e.g., *Mackas*, 2006] as well as ocean climate variability and influences on coastal communities, storms, and the carbon budget.

[5] This paper presents a few aspects of the surface currents off the USWC which are newly observable as a result of the operation of the HFR network (Figure 1a): variance of surface currents (section 3.1), poleward propagating alongshore surface currents (section 3.2), demography of submesoscale eddies (section 3.3), and scale continuity in the power law spectra (section 3.4).

2. Data Analysis

2.1. HFR-Derived Surface Currents

[6] The radial velocity maps derived by 61 HFRs (as of January 2009) on the USWC are optimally interpolated on equally spaced grid points with 6 km resolution to generate vector current maps and other kinematic and dynamic quantities (stream function, velocity potential, divergence, vorticity, and deformation rate) as well as their uncertainty estimates [e.g., *Kim et al.*, 2008; *Kim*, 2010; *Terrill et al.*, 2006] (Figure 1a). All HFRs used in this analysis are built on the commercially available compact antenna system (CODAR Ocean Sensors, Palo Alto, California) and are locally calibrated using antenna beam pattern measurements. An isotropic exponential correlation function with 10 km decorrelation length scale was used to objectively map from radials to the vector current field, with assumed error and model standard deviations of 6 and 40 cm s^{-1}, respectively. The surface current products discussed are insensitive to the choice of model and error variances. As a minor note on the data processing, the radial velocity map from each HFR has its own spatial resolution in the range and azimuthal directions depending on both radar operating frequency and sweeping frequency. Since the radial velocities with higher spatial resolution are likely to produce a bias in the vector current map, radial velocity maps are bin averaged to make them comparable in resolution (e.g., 3–5 km range and 5° azimuthal resolutions) before they are optimally interpolated.

[7] The uncertainty of HFR surface current measurements has been estimated with independent in situ observations from ADCPs, radial velocities of multiple HFRs, and GPS-tracked drifters, with typical ranges, respectively, of 5–19 cm s^{-1} [e.g., *Shay et al.*, 1995; *Emery et al.*, 2004; *Kaplan et al.*, 2005], 5–7 cm s^{-1} [e.g., *Kim et al.*, 2008], and 1–10 cm s^{-1} [e.g., *Ohlmann et al.*, 2007]. In the present analysis, the uncertainty is computed using currents at the uppermost bin of in situ ADCPs (National Data Buoy Center (NBDC) buoys 46027, 46011, 46063, and 46053, moorings at Orange County Sanitation District (OCSD), Point Loma Ocean Outfall (PLOO), and International Boundary and Water Commission (IBWC)), located mostly in southern California. The estimated uncertainty ranges from 4 to 12 cm s^{-1} depending on the depth of the uppermost bin in the subsurface current observations, geometry of the installed radars, and radar operating frequency. As the uppermost bin is near the surface, the root-mean-square (RMS) difference becomes smaller.

2.2. Spatial and Temporal Coverage

[8] Spatially contiguous surface current maps spanning the entire California and Oregon coastlines have only been available since August 2008, when the radar system at Shelter Cove, California became operational. Thus, the long-term/seasonally averaged current field in this region can be biased and have higher statistical uncertainty due to insufficient realizations. The effective spatial coverage of the USWC HFRs is defined as the area with at least 90% data availability for 5 months (August to December of 2008), and is outlined by a blue curve in Figure 1a. The baseline, the straight line between two radar sites, is an area where it is not possible to estimate vector solutions from nearly parallel radial velocities as they weakly constrain the vector solutions normal to the baseline. Therefore the vector solutions along the baseline could be anomalous or discontinuous when only two sites cover the baseline and appear as higher variance (e.g., between San Clemente Island and San Diego). In other words, the baseline is the area with high geometric dilution of precision (GDOP) [e.g., *Levanon*, 2000; *Kim et al.*, 2008]. Although optimal interpolation eliminates baseline artifacts, it also requires information to determine the vector current solution near the baseline.

[9] In addition, the radar beam pattern imposed on the operation of each radar might generate another bias on the vector current field. The along-coast fractional total data availability (β_A) of surface vector currents over 2 years is shown in Figure 1c, which can be an indicator of the density of overlapped radial maps.

2.3. Power Spectra

[10] The rotary spectra and polarization coefficients (Figures 1b, 2a, and 2b) are calculated from surface vector currents over the entire domain in Figure 1a. A single time series is broken into 30 nonoverlapped time series with identical record lengths in order to acquire degrees of free-

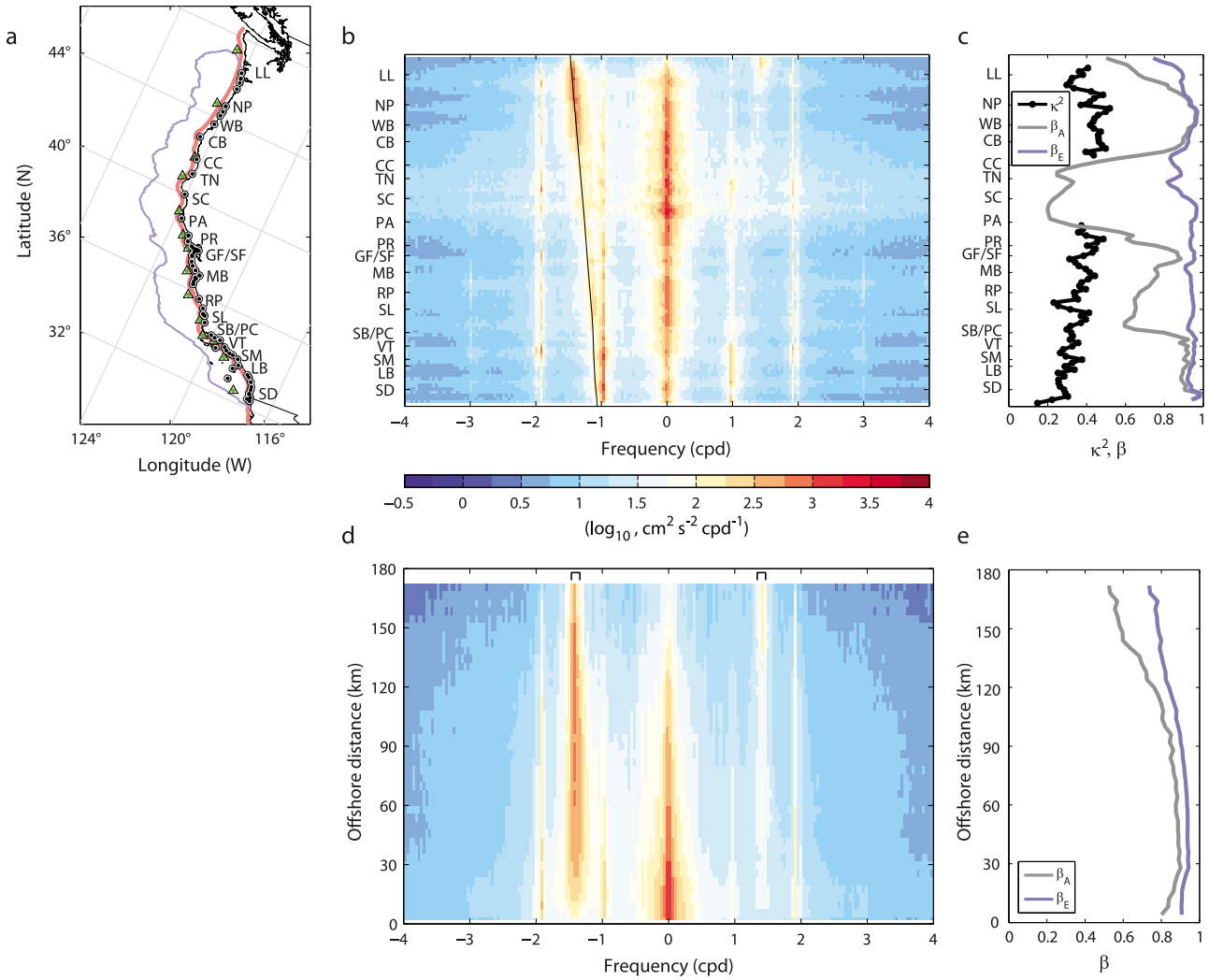

Figure 1. (a) High-frequency radar (HFR) network on the USWC for surface current observations (61 HFRs are marked as black dots as of January of 2009). The blue curve indicates the effective spatial coverage of surface current map over 2 years (2007 and 2008), and a red curve denotes the coastline axis. For the wind regression analysis, coastal winds at 14 National Data Buoy Center (NDBC) buoys (triangles with a green dot) are used. As a reference, major coastal regions are denoted by abbreviated two letter names from south to north: San Diego (SD), Long Beach (LB), Santa Monica (SM), San BuenaVentura (VT), Santa Barbara (SB), Point Conception (PC), Port San Luis (SL), Ragged Point (RP), Monterey Bay (MB), Gulf of the Farallones (GF), San Francisco (SF), Point Reyes (PR), Point Arena (PA), Shelter Cove (SC), Trinidad (TN), Crescent City (CC), Cape Blanco (CB), Winchester Bay (WB), Newport (NP), and Loomis Lake (LL). (b) Rotary power spectra ($\log_{10}$ scale, $cm^2\ s^{-2}\ cpd^{-1}$) of surface vector currents in the entire domain as a function of frequency (cpd) and coastal regions on the USWC, averaged in each frequency bin and alongshore bin. A black curve indicates the inertial frequency. (c) Wind skill (κ^2), the fraction of variance explained by coastal surface winds at the NDBC buoys through linear regression, and the fractional data availability (β) of surface currents over 2 years. A simple ratio (β_A) of the number of observations to the entire time period and the conditional data availability (β_E) as the fraction of vector current data participating in the estimate of spectra are shown (sections 2.2 and 2.3). The wind skill between PA and CC is excluded due to lack of concurrent observations of coastal winds and surface currents on the coastline axis in Figure 1a. (d) Rotary power spectra ($\log_{10}$ scale, $cm^2 s^{-2}\ cpd^{-1}$) of surface vector currents off Oregon and southern Washington (north of 42°N or Crescent City) as a function of frequency and offshore distance (km). A range of the local inertial frequency is shown as black brackets. Figures 1b and 1d share the same color bar. (e) Fractional data availability (β_A and β_E) of surface currents in the north of 42°N.

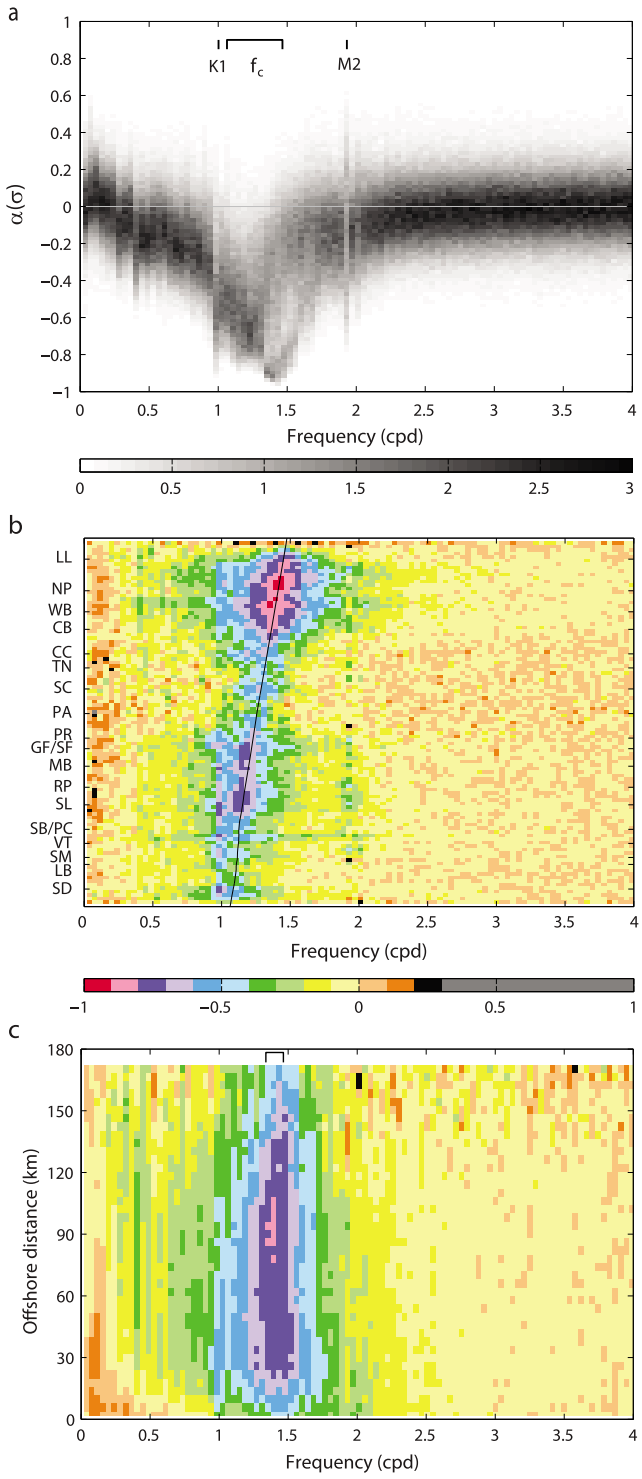

Figure 2. (a) A probability density function of polarization coefficients at each frequency bin. The range of the inertial frequency (f_c) and two tidal frequencies (K_1 and M_2) are indicated. (b) Polarization coefficients averaged in each frequency bin and alongshore bin. A black line indicates the local inertial frequency. (c) Polarization coefficients of surface currents off Oregon and southern Washington (north of 42°N or CC) as a function of frequency and offshore distance (km). A range of inertial frequency is shown as a black bracket. Figures 2b and 2c share the color bar.

dom for spectral analyses [e.g., *Priestley*, 1981; *von Storch and Zwiers*, 1999; *Kim et al.*, 2010a], then the spectra estimates for individual segments are averaged. If the number of missing observations is more than 50% of the length of each chunk, the segment is not included in the estimate of spectra. Here, the conditional data availability (β_E) is defined as the fraction of vector current data participating in the estimate of spectra (Figure 1c), which are based on at least 80% observations and 20 segments.

[11] For the alongshore plots (Figures 1b, 2b, and 3), all grid points (8527 grid points) in the domain are mapped to a grid following the coastline orientation and computing the alongshore distance from the south end. Then, the rotary spectra and polarization coefficients are averaged in each frequency bin ($\Delta\sigma$ = 0.0411 cpd) and alongshore bin (Δl = 20 km). The coastline axis is designed as a spline curve having 20 km resolution approximately 15 to 20 km seaward of the shoreline and is chosen to pass through the Santa Barbara Channel and the San Pedro Channel in southern California (red curve in Figure 1a). The noise level of the surface current power spectrum varies along the coast due to differences in the regional sea states which control the Bragg scatter of the radio signal, and to variations in how each individual HFR system operated (Figure 1b). In a similar way, the cross-shore presentation of power spectra and polarization coefficients is shown as a function of offshore distance (Figures 1d and 2c). Although defining the offshore distance in coastal regions off southern California and in the Gulf of the Farallones can be complicated due to islands, most iso-offshore contours are parallel to the coastline. As surface currents off Oregon and southern Washington (north of 42°N or Crescent City) have strong signal-to-noise ratio of inertial energy and well capture common features of surface currents off the USWC in the cross-shore direction, we present their spectra and polarization coefficients as a presentation of variance in the cross-shore direction. Moreover, the fractional availably as a function of offshore distance of surface currents in this region is shown in Figure 1e.

2.4. Tide Coherent Currents

[12] The tide coherent surface currents are referred to as the surface currents at major tidal frequencies (M_2, K_1, S_2, O_1, N_2, and P_1 but not S_1; see below), and they are computed using harmonic analysis [e.g., *Pawlowicz et al.*, 2002; *Kim et al.*, 2010a]. Variance at S_1 frequency is retained in the detided data as it is assumed to be primarily due to diurnal land/sea breeze forcing, given that model estimates of S_1 barotropic tidal currents are very weak: 0.08 to 0.17 cm s^{-1} [e.g., *Ray and Egbert*, 2004]. For comparison with barotropic tidal models [*Spargo et al.*, 2004; *Egbert et al.*, 1994] and observed tidal surface currents (Figure 3), the amplitude and phase at K_1 and M_2 frequencies of tidal models are estimated on the grid points of HFR surface currents. Alongshore distribution of their mean and RMS is computed in the same way of rotary power spectra (Figures 1b and 3).

2.5. Wind Regression

[13] The wind transfer functions (**H**, Figure 4) are derived from regression of Fourier coefficients of observed NDBC

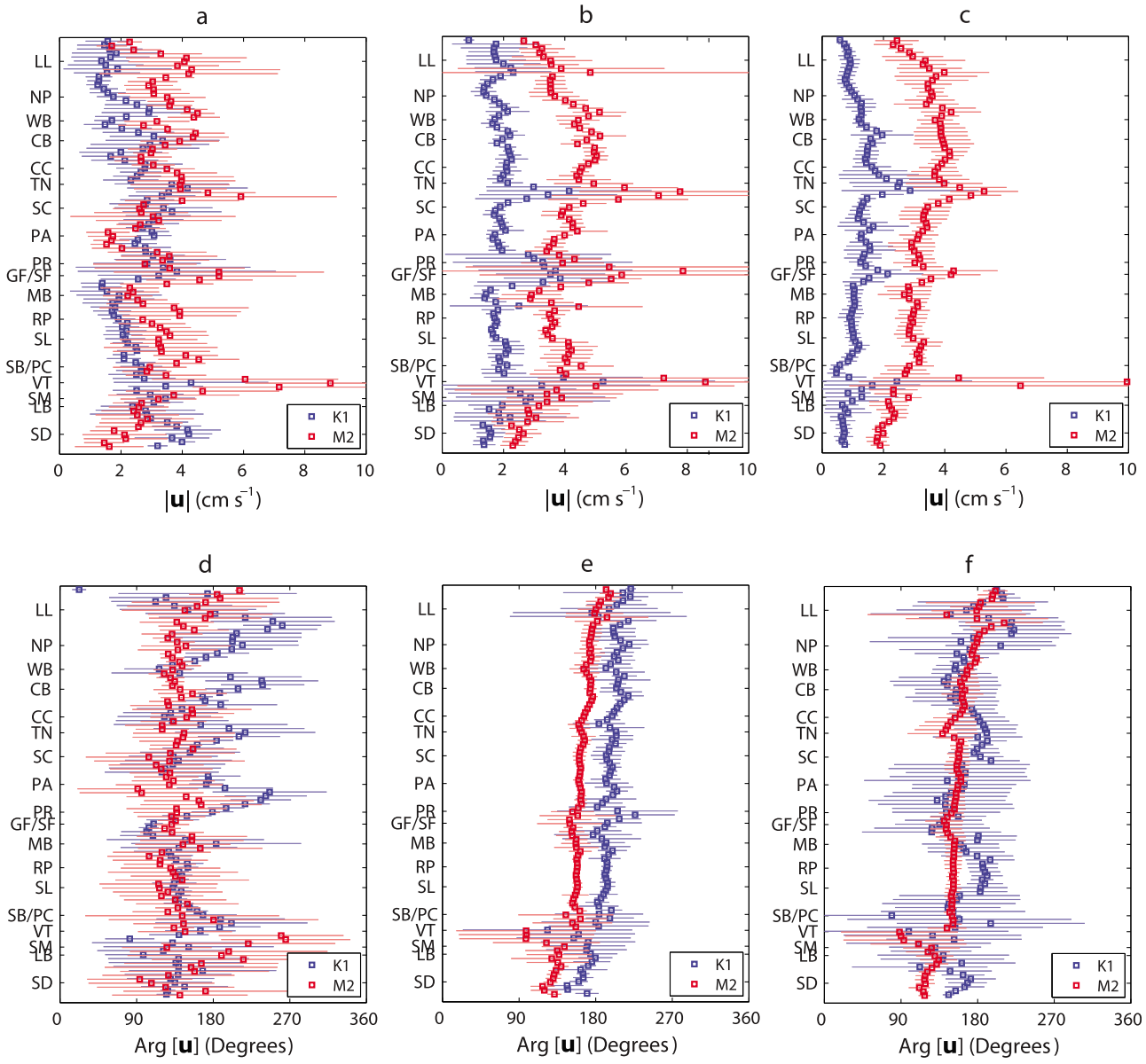

Figure 3. Alongshore distribution of the amplitude and phase of K_1 and M_2 (surface) currents (**u**) observed from the HFR network off the USWC (Figures 3a and 3d) and derived from nearshore (ENPAC 2003: Figures 3b and 3e [*Spargo et al.*, 2004]) and global (TPXO v7.2: Figures 3c and 3f [*Egbert and Erofeeva*, 2002]) barotropic tidal models. (a–c) Amplitude (cm s^{-1}). (d–f) Phase (degrees). The mean and RMS of the amplitudes and phases in each alongshore bin are presented as squares and error bars, respectively. The outputs of tidal models are mapped on the grid points within the effective coverage of surface currents (blue curve in Figure 1a).

coastal vector winds ($\hat{\boldsymbol{\tau}}$) and nearby detided surface vector currents ($\hat{\mathbf{u}}_F$):

$$\mathbf{H}(l,\sigma) = \left(\langle \hat{\mathbf{u}}_F(l,\sigma)\hat{\boldsymbol{\tau}}^\dagger(l_*,\sigma)\rangle\right)\left(\langle \hat{\boldsymbol{\tau}}(l_*,\sigma)\hat{\boldsymbol{\tau}}^\dagger(l_*,\sigma)\rangle + \mathbf{R}\right)^{-1}, \tag{1}$$

where **R** is the regularization matrix to suppress the noise in the wind stress and to tune variance of the regression estimate (see *Kim et al.* [2009a, 2010b] for more details) († denotes the complex conjugate transpose). The isotropic transfer functions are computed from a pair of surface currents ($\mathbf{u} = u + iv$) on the coastline axis (l) and coastal winds ($\boldsymbol{\tau} = \tau_x + i\tau_y$) at a nearby buoy ($l_*$) (Figure 4).

[14] The wind skill (κ^2, Figure 1c), the fraction of variance of surface currents explained by the coastal surface winds, is computed using multiple regression bases such as winds at 14 NDBC buoys ($N = 14$ in equation (3)) to capture variability ranging from large-scale wind setup to local winds (Figure 1a).

$$\kappa^2 = 1 - \frac{\langle(\hat{\mathbf{u}}_F - \hat{\mathbf{u}}_W)^2\rangle}{\langle \hat{\mathbf{u}}_F^2\rangle}, \tag{2}$$

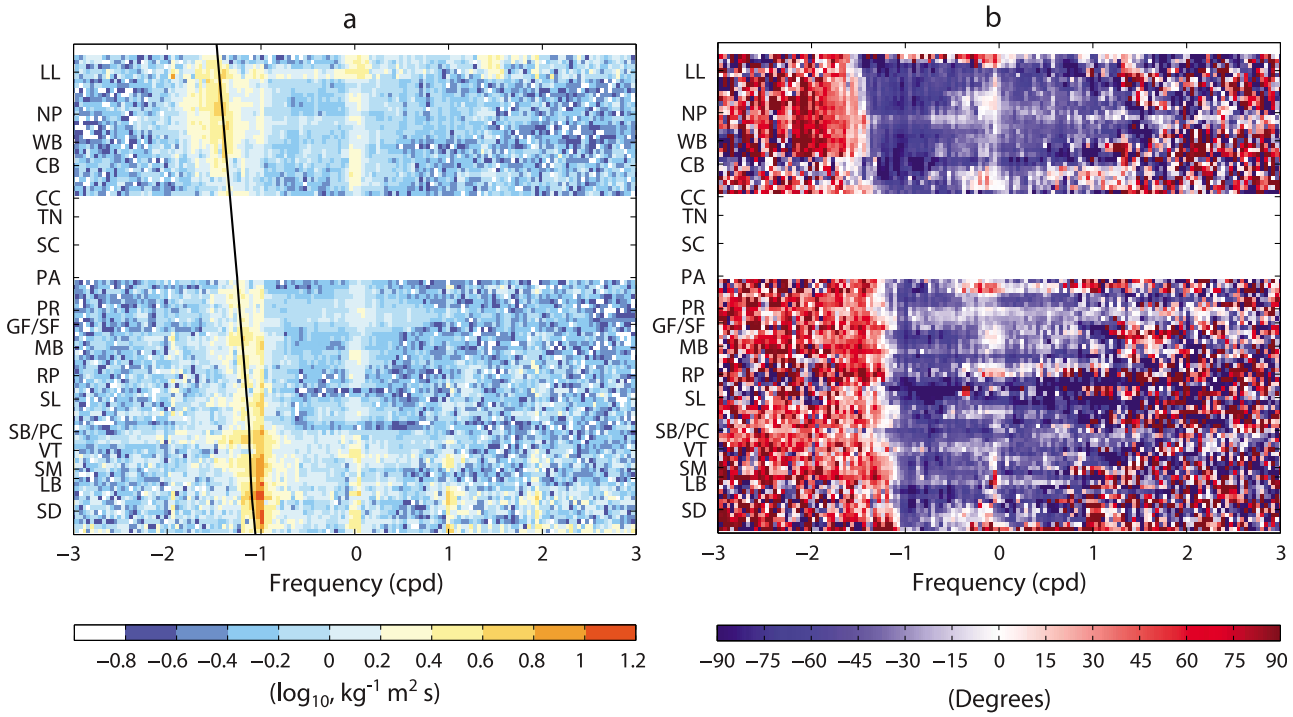

Figure 4. The USWC-wide isotropic wind transfer function. (a) Magnitude ($\log_{10}$ scale, kg^{-1} m^2 s). A black line indicates the inertial frequency. (b) Argument (degrees). The estimates between PA and CC are excluded due to lack of concurrent observations of coastal winds and surface currents (Figure 1c).

where $\hat{\mathbf{u}}_W$ is the Fourier coefficients of wind coherent surface currents, presented as

$$\hat{\mathbf{u}}_W(l,\sigma) = \sum_{n=1}^{N} \mathbf{H}_n(l,\sigma)\hat{\boldsymbol{\tau}}_n(l_*,\sigma). \tag{3}$$

Thus, local and remote winds in this paper are referred to as the winds inside and outside of the USWC region, respectively. In the wind regression analysis, since concurrent observations of coastal winds and surface currents are required, the wind skill and transfer function in part of northern California is not included due to insufficient data overlap (Figures 1c and 4). Moreover, to make most use of partially missing data in the multiple bases, the data covariance matrix is computed with a modified expectation maximization [e.g., *Schneider*, 2001].

2.6. Subinertial Alongshore Surface Currents

[15] The surface currents on the coastline axis are computed from local averaging of 6 km resolution data within a 20 km diameter from a grid point on the coastline axis in order to increase SNR of variance in near-coast surface currents. The alongshore and cross-shore current components are computed by projecting the current vector to the coastline axis (Figure 5). The subinertial surface currents are filtered to daily-averaged surface currents (Figures 5a and 5b).

2.7. Comparison of Power Spectra

[16] To compute the statistics of submesoscale eddies off the entire USWC over 2 years (Figure 6), the stream function and vorticity field are used to detect subinertial circular flows. Using flow geometry, a set of nearly enclosed streamlines with persistent vorticity for at least two days is identified as an eddy. As this approach is only suitable to circular flows with approximate diameter less than 100 km, large mesoscale eddies such as Mendocino eddy are not included in this analysis. The applied eddy detection technique is examined thoroughly by *Kim* [2010].

[17] The power spectra of satellite altimetry-derived (ALT) geostrophic currents are calculated using along-track sea level anomalies (SLAs) from two satellites (Envisat and Jason-1). The spectrum of along-track SLAs is converted into that of geostrophic currents by taking an along-track derivative [e.g., *Stammer*, 1997]:

$$S_{\mathbf{u}_\perp}(k_\parallel) = \left(\frac{g}{f_c}\right)^2 (2\pi k_\parallel)^2 S_{\eta_\parallel}(k_\parallel), \tag{4}$$

where $\eta_\parallel$, $k_\parallel$, g, and f_c denote the along-track SLAs, along-track wave number, gravitational acceleration, and local inertial frequency, respectively (Figure 7a). For the frequency domain estimate, the cross-track currents ($\mathbf{u}_\perp$) are averaged within 2-degree square boxes and by month in order to generate a time series (Figure 7b):

$$\mathbf{u}_\perp(t) = \frac{g}{f_c}\frac{\Delta\eta_\parallel(t)}{\Delta l}. \tag{5}$$

[18] Variance of (surface) currents varies with sampling location because of regional variations in driving forces and geostrophic components. In the comparison of spectra of ALT- and HFR-derived currents, the HFR surface currents

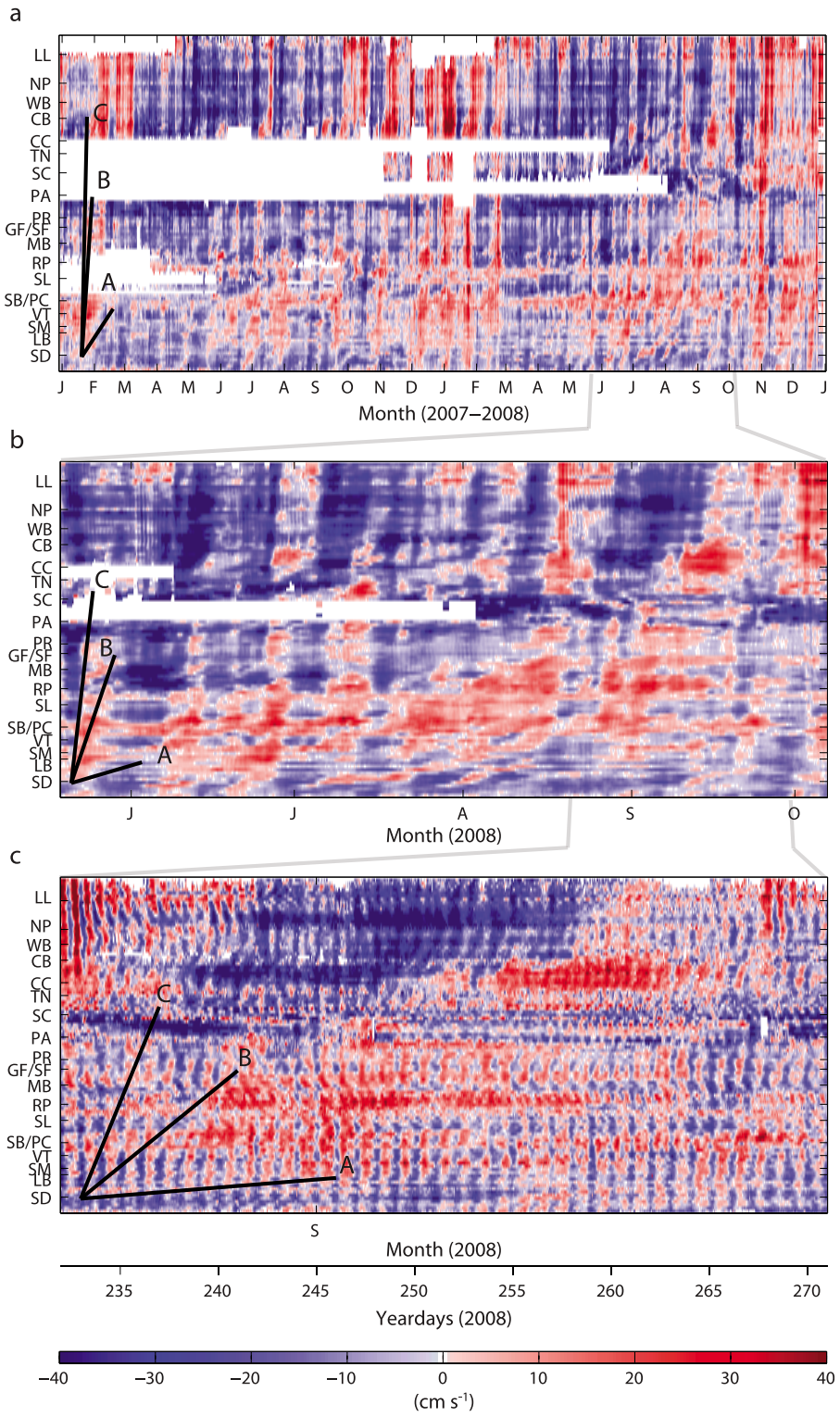

Figure 5. (a and b) Time-alongcoast diagram of subinertial alongshore surface currents (cm s^{-1}) for 2 years (2007 and 2008) and about 5 months of 2008 (May 20 to October 10), respectively. Red and blue colors indicate the poleward (upcoast) and equatorward (downcoast) currents. The missing observations are presented with white space. Three black lines indicate the reference phase speeds of 10 (A), 100 (B), and 300 (C) km day^{-1}. (c) Time-alongcoast diagram of hourly alongshore surface currents (cm s^{-1}) on year days 232 to 271 of 2008 (August 20 to September 28). The first day of each month is labeled.

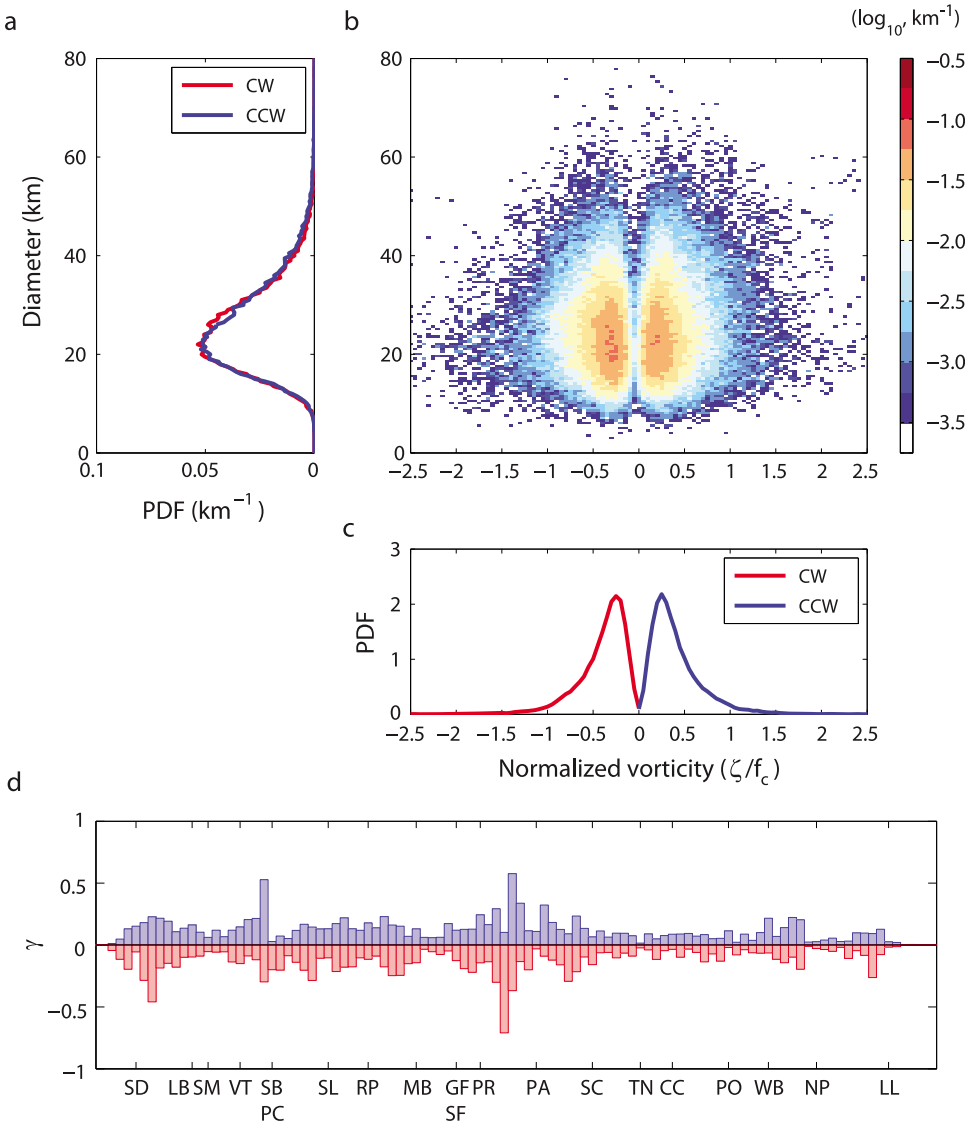

Figure 6. (a–c) Probability density functions of diameters of identified eddies (Figure 6a) and Rossby number ($R_o = \zeta/f_c$) at the center (Figure 6c) and their joint probability density function (Figure 6b). The bin size of the diameter and normalized vorticity is 0.5 km and 0.05, respectively. (d) Relative occurrence index (γ) of submesoscale eddies off the USWC, which reflects the effective data availability (β_A, Figure 1c). The red and blue color bars indicate clockwise ($\gamma < 0$) and counterclockwise ($\gamma > 0$) rotations, respectively.

with resolutions of 1 km and 6 km are sampled along a zonal grid line off southern San Diego and in the area between Los Angeles and San Diego, respectively, where there are relatively weak winds (Figure 1c). The HFR surface currents of 20 km resolution on the coastline axis are constructed to capture the largest spatial scales on the USWC (Figures 1a and 7a). On the other hand, the along-track SLAs are taken from sloping tracks in the northeastern Pacific (30°N to 50°N, 114°W to 133°W). To minimize the influence of missing observations on the spectrum estimates, a weighted least squares fit is used. The HFR surface currents at 20 km resolution are only available from August to December of 2008, so the wave number spectrum is computed from only 5 months of data. This selective estimate does not change overall results. The errors of power spectrum estimates are shown by the 95% confidence interval (Figure 7).

3. Results

3.1. Variance of Surface Currents

[19] The spectra of surface vector currents off the USWC are characterized by variance peaks in the low-frequency band [$|\sigma| \leq 0.4$ cycles per day (cpd)], in two bands centered at diurnal and semidiurnal frequencies [tides (K_1, M_2, and S_2), diurnal wind (S_1) and its harmonics], and at the inertial frequency (f_c = 1.06 to 1.49 cpd for 32°N to 48°N) (Figures 1b and 7b) [e.g., *Paduan and Rosenfeld*, 1996; *Kosro*, 2005; *Beckenbach and Washburn*, 2004; *Kaplan et al.*, 2005; *Gough et al.*, 2010; *Kim et al.*, 2010a].

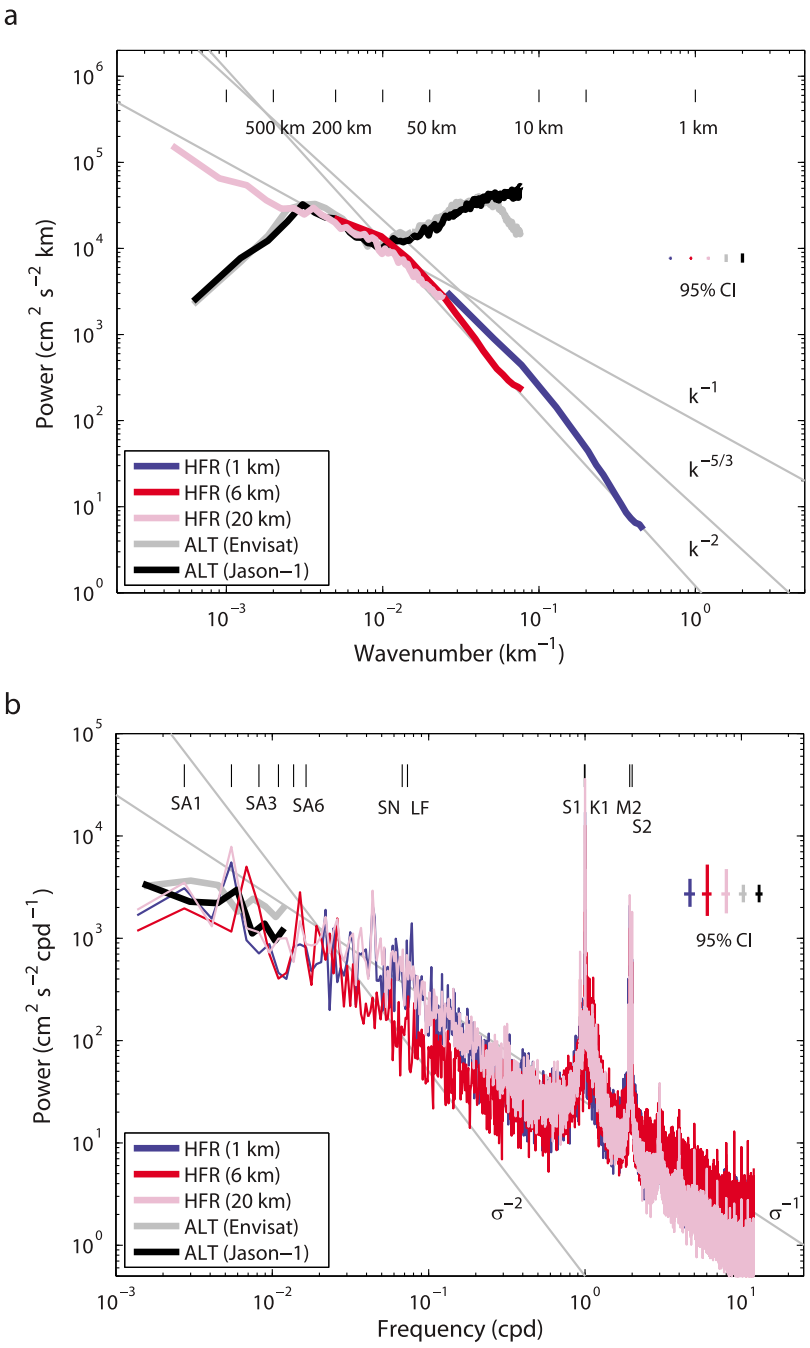

Figure 7. Power spectra of high-frequency radar-derived (HFR; 1, 6, and 20 km resolutions) surface currents and altimeter-derived geostrophic currents (ALT; along-track Envisat and Jason-1) for 2 years (2007 and 2008) in the (a) wave number domain (length scales (L) of 1, 5, 10, 50, 100, 200, 500, and 1000 km are marked) and (b) frequency domain (six seasonal harmonics (SA_1 to SA_6), spring-neap (SN, 14.765 day), lunar fortnightly (LF, 13.661 day), S_1, K_1, M_2, and S_2 tidal frequencies are marked). The auxiliary lines are denoted as k^{-1}, $k^{-5/3}$, and k^{-2} in the wave number domain and σ^{-1} and σ^{-2} in the frequency domain. The 95% confidence interval (CI) of individual spectra is indicated.

[20] The inertial variance of surface currents increases to the north, due in part to the response to increasingly strong winds and to energetic nonlinear interactions due to decreasing baroclinic Rossby deformation radius and increasing intermittency [e.g., *Munk and Phillips*, 1968; *Stammer*, 1997; *Chelton et al.*, 1998]. The presence of variance in the counterclockwise inertial band (positive frequency axis) implies elliptical motions of near-inertial surface currents rather than pure circular motions. This succinct view of surface current energy enables us to identify possible driving forces for the surface circulation such as local and remote winds, tides, low-frequency pressure gradients, and baroclinic motions due to coastal boundaries

(e.g., capes, headlands, and bays) and changing bottom topography.

[21] In the cross-shore direction, variance of surface currents show the influence of the coastal boundary, which may be due to both shallow depth and no-flow boundary condition (Figure 1d). Variance at low frequency and tidal frequencies offshore decreases. Low-frequency energy trapped near the coast and amplified tidal motions over the continental shelf are expected and scattering and baroclinic motions due to the interaction with bottom bathymetry and coastal boundary are larger than offshore. However, clockwise inertial variance transits from weak inertial energy (less than 20 km from the coast, $d < 20$ km) to a broad inertial peak (20 km $\leq d < 80$ km) and a narrow inertial peak ($d \geq 80$ km) (Figures 1d and 2c). The clockwise inertial circular motions are restricted near the coast but not offshore in a similar way. In addition, the counterclockwise inertial motions appear from 100 km offshore ($d \geq 100$ km). Considering the narrow inertial peak offshore and its increasing tendency, the influence of missing observations (β_E in Figure 1e) will be negligible in spectra estimates.

3.1.1. Tide Coherent Surface Currents

[22] The polarization coefficient (α) describes the sense of rotation of currents in each frequency band as clockwise ($\alpha < 0$) or counterclockwise ($\alpha > 0$):

$$\alpha(\sigma) = \frac{-S_\circ(\sigma) + S_\bullet(\sigma)}{S_\circ(\sigma) + S_\bullet(\sigma)}, \tag{6}$$

where $S_\circ$ and $S_\bullet$ are clockwise and counterclockwise variances, respectively.

[23] The highly spread polarization at diurnal (K_1, σ = 1.0027 cpd) and semidiurnal (M_2, σ = 1.932 cpd) frequencies indicate the partial influence of the diurnal sea/land breezes (S_1, σ = 1 cpd) and the coexistence of barotropic and baroclinic tide coherent surface current components, respectively (Figure 2a). Those components can be distinguished by differences in their spatial structure [e.g., *Kaplan et al.*, 2005; *Rosenfeld et al.*, 2009], even though the measured currents are averages of only the upper $O(1)$ m depth.

[24] The K_1 and M_2 tide coherent surface currents are compared with barotropic tidal currents derived from ENPAC 2003 nearshore and TPXO global tidal models [e.g., *Spargo et al.*, 2004; *Egbert et al.*, 1994]. Although the phase is more sensitive than the amplitude is, both are similar to the models in terms of magnitude and alongshore pattern (Figure 3). For instance, the strong variance of M_2 surface currents off Oregon, Bodega Bay, Gulf of the Farallones, Monterey Bay, Santa Monica, and Ventura agrees well. However, the K_1 surface currents are not purely tidal because they can include variance driven by both lunisolar diurnal tide (K_1 tide) and seasonal harmonics of diurnal winds ($1 \pm \Delta\sigma$, $\Delta\sigma$ = 1/365.2425 days = 0.0027 cpd). Thus the amplitude appears approximately 30 to 50% more than that in models, and the phase in observations has 2 to 3 times more RMS as local fluctuations. The local structure of the M_2 surface currents (not shown) suggests the influence of bottom topography and Coriolis force [e.g., *Rosenfeld and Beardsley*, 1987]. It can be related to the surface signature of M_2 internal tides as persistently observed in the coastal areas noted above [e.g., *Erofeeva et al.*, 2003; *Kaplan et al.*, 2005; *Rosenfeld et al.*, 2009; *Gough et al.*, 2010].

3.1.2. Wind Coherent Surface Currents

[25] The current response to the wind in coastal regions can be anisotropic and asymmetric, in contrast to the isotropic response in the open ocean, because the geostrophic balance with local pressure setup against the coast in the cross-shore direction and the frictional balance with wind stress in the alongshore direction are not symmetric [e.g., *Ekman*, 1905; *Allen*, 1980; *Huyer and Kosro*, 1987; *Overland and Pease*, 1988; *Kim et al.*, 2009a]. For example, onshore and offshore winds generate different and asymmetric wind-driven responses due to a coastal boundary. A statistical regression of wind on coastal surface currents, allowing anisotropy and asymmetry, provides a framework to describe their relationship and a basis to build stochastic models for forecast and hindcast [e.g., *Chelton et al.*, 1988; *Kim et al.*, 2010a, 2010b]. However, the isotropic transfer function is more routine and effective to present the relationship between wind and currents than the anisotropic transfer function. The USWC-wide isotropic wind transfer function contains two primary peaks at the inertial frequency and low frequency, interpreted as the wind current dynamics and the influence of the coastal boundary (Figure 4) [e.g., *Ekman*, 1905; *Gonella*, 1972; *Kim et al.*, 2009a].

[26] The wind skill ranges from 0.2 to 0.5 and increases from southern California to Oregon and Washington (Figure 1c), which is aligned with the RMS of alongshore coastal winds: even the decreasing tendency to the north of Newport, Oregon [e.g., *Dorman and Winant*, 1995]. One possible explanation of the decreasing skill is the seasonally alternating setup of remote and local winds between northern California and Oregon/Washington, which generate disparate variability on both sides [e.g., *Chelton and Davis*, 1982; *Battisti and Hickey*, 1984]. A similar analysis with the wind at NDBC buoys and detided sea surface heights (sea surface height anomalies, SSHAs) off the USWC shows the consistent pattern of wind skill. As winds at multiple buoys are used as the regression basis, the local and remote responses should correspond to components coherent with winds within and outside the USWC, respectively, in spite that this analysis is subject to the limitations of regression.

3.1.3. Surface Currents at Low Frequency

[27] Polarization coefficients of currents forced by wind (Ekman model) and by pressure perturbation (internal waves) without friction are

$$\alpha(\sigma) = \begin{cases} -\dfrac{\sigma}{f_c} & : \quad 0 \leq \sigma < f_c \\ -\dfrac{f_c}{\sigma} & : \quad \sigma \geq f_c, \end{cases} \tag{7}$$

$$\alpha(\sigma) = \frac{-2\sigma f_c}{\sigma^2 + f_c^2}, \tag{8}$$

respectively [e.g., *Fofonoff*, 1969; *Gonella*, 1972; *LeBlond and Mysak*, 1978]. Currents in the northern hemisphere have clockwise dominance with a tendency of no rotational preference at zero frequency [$\alpha(\sigma \to 0) \to 0$], pure clockwise motions at the inertial frequency [$\alpha(f_c) = -1$], and nearly equal polarization [$\alpha(\sigma \to \infty) \to 0$] at higher frequencies (Figure A1).

[28] Positive polarization in the very low frequency band ($\sigma \leq 0.2$ cpd) is mainly attributed to persistent eddies and meanders offshore and coastal boundary effects nearcoast (Figures 2a and A1). Persistent counterclockwise eddies off Santa Barbara Channel, Bodega Bay, and Long Beach (Oregon), meandering jets and currents with the same rotational tendency between Point Reyes to Cape Blanco [e.g., *Strub et al.*, 1991], the equatorial jet and its separation due to topography near Stonewall Bank [e.g., *Castelao and Barth*, 2005] are observed (not shown).

[29] On the other hand, the wind-driven currents constrained by the coastal boundary have counterclockwise polarization in the subinertial frequency band (Figures 2c and A1), because the influence of the coastal boundary is partially manifested as counterclockwise currents with red spectra. Positive polarization appears in the nearcoast region between San Diego and Santa Monica, in northern California, and in Oregon.

3.2. Alongshore Surface Currents

[30] A time-alongcoast diagram of subinertial alongshore surface currents shows two types of poleward propagating signals with phase speeds of $O(10)$ and $O(100$ to $300)$ km day^{-1} similar to typical shelf mode speeds [e.g., *Chapman*, 1987; *Ramp et al.*, 1997]. The spring and fall transitions relating to the onset and demise of seasonal upwelling-favorable winds are also visible, most prominently off central and northern California [e.g., *Strub et al.*, 1987; *Largier et al.*, 1993; *Kaplan et al.*, 2005; *Kosro*, 2005] (Figures 5a and 5b).

[31] Frequently, poleward propagating signals with time scales of 2 to 3 weeks are visible as tilted dark red or blue stripes denoting upcoast and downcoast surface currents (Figure 5). One mechanism for poleward signals is CTWs, which are a hybrid of barotropic continental shelf waves and internal Kelvin waves [e.g., *Chapman*, 1987; *Brink*, 1991; *Ramp et al.*, 1997]. Slower-propagating (higher mode) alongshore currents are observed principally in southern California. As higher mode CTWs are more sensitive to bottom topography, it is hypothesized that the reduction of energy to the north is due to reflection and scattering by the abrupt change of coastline curvature near Point Conception, California [e.g., *Ramp et al.*, 1997; *Grimshaw and Allen*, 1988; *Wilkin and Chapman*, 1990]. The spatial and time-lagged correlation of alongshore surface currents and the two-dimensional spectra in wave number and frequency domains confirm the observed two phase speeds, which agree with the results from a two-dimensional linear CTW model [e.g., *Brink et al.*, 1987; *Brink and Chapman*, 1987].

[32] As a complementary observation off the USWC [e.g., *Halliwell and Allen*, 1984; *Spillane et al.*, 1987], SSHAs off the USWC show propagating features along the coast with time scales of 2 to 3 weeks as poleward (May to August), equatorward (December to April), and alternating direction during the rest of the year. Although the propagating signals of SSHAs are coherent with those of alongshore coastal winds, they are not always matched with HFR surface currents (not shown).

[33] Alongshore surface currents demonstrate the wind-driven seasonal circulation as an equatorward flow in response to upwelling-favorable winds in spring and poleward currents with wind relaxation in fall [e.g., *Largier et al.*, 1993; *Strub and James*, 2000; *Kosro*, 2005]. However, after removing wind-driven currents using regression analysis (section 3.1.1 and Figure 1c), the residual surface currents still contain persistent poleward propagating features, suggesting that some poleward events near the coast are influenced by remote forcing [e.g., *Davis and Bogden*, 1989]. Similarly, poleward signals forced by local and remote winds are reported in the SSH field on the USWC.

[34] Moreover, this USWC-wide view of alongshore currents has areas of divergence and convergence in alongshore surface transport, related to alongshore differences in the wind field [e.g., *Largier et al.*, 1993; *Kaplan et al.*, 2009]. This divergence/convergence influences upwelling and transport pathways, and thus is critical to plankton ecology. An example of the poleward progression of the convergence front in unprecedented detail (on year days 242 to 260 of 2008 from San Francisco to Newport) is presented with hourly alongshore surface currents (Figure 5c). This example demonstrates how the ensemble of HFR observations constitutes a new and unique resource for coastal oceanography and ecosystem management.

3.3. Demography of Submesoscale Eddies

[35] About 2200 identified eddies with clockwise and counterclockwise rotations with at least two-day persistence, respectively, show similar statistics as Rossby numbers ($R_o = \zeta/f_c$, where ζ is vertical component of relative vorticity at the center of the eddy; $\zeta = \partial v/\partial x - \partial u/\partial y$) of 0.1 to 3 and diameters in the range of 10 to 60 km (Figures 6a to 6c). They persist for up to 12 days and drift northward and westward dominantly with a speed of 10 to 60 cm s^{-1}. More than 70% of identified eddies are found within 80 km from the coast.

[36] The relative occurrence index (γ) shows the ratio of the number of days that eddies are observed over the entire time period by reflecting missing observations (Figure 6d), defined as

$$\gamma(l) = \frac{c(l)}{\beta_A(l)}, \tag{9}$$

where $c(l)$ and $\beta_A(l)$, respectively, are the number of days when eddies are observed and the total data availability in a given alongshore location (l) (Figure 1c).

[37] The most persistent submesoscale eddies are found in the Santa Barbara Channel and between Point Reyes and Point Arena [e.g., *Nishimoto and Washburn*, 2002; *Beckenbach and Washburn*, 2004]. Instability of shear flow and horizontal density gradients are expected to generate submesoscale eddies. Island wakes, terrain-following flows at points and their lee, and horizontal shear due to countercurrents nearshore have been observed [e.g., *Wolanski et al.*, 1984; *Caldeira et al.*, 2005].

[38] The vertical secondary circulation associated with submesoscale eddies plays an important role in the vertical flux of mass, buoyancy, and potential vorticity in the upper ocean and in changing the structure of the mixed layer and upper ocean stratification [e.g., *Capet et al.*, 2008; *Klein and Lapeyre*, 2009; *Kim*, 2010].

3.4. Scale Continuity

[39] The continuity of the power spectra of ocean currents from submesoscale to mesoscale is investigated by

comparing energy in the wave number ($k = 1/L$) and frequency ($\sigma = 1/T$) domains.

[40] The wave number spectra of HFR surface currents show a consistent and continuous variance distribution across three different resolutions (1, 6, and 20 km) (Figure 7a). Resolved scales range from $O(1000)$ km to $O(1)$ km, and the spectra decay with k^{-2} at high wave number in agreement with theoretical submesoscale spectra [e.g., *McWilliams*, 1985; *Capet et al.*, 2008]. Although their spectra can vary with location because of regional variations in driving forces and geostrophic contents, they have a robust k^{-2} decay. Moreover, HFR observations resolve variability at scales smaller than about 100 km, where the noise in satellite altimeter-derived (ALT) currents becomes dominant over oceanic signals [e.g., *Stammer*, 1997]. For example, the wave number spectra of HFR surface currents in a region (e.g., southern California) with minimum wind-driven components (Figure 1c) are comparable to the spectra of along-track ALT geostrophic currents (Envisat and Jason-1) in the northeastern Pacific (30°N to 50°N, 114°W to 133°W). The mismatch at low wave number ($L > 500$ km) is likely due to differing coverage (e.g., coastal regions versus open ocean): HFR surface currents contain alongshore coastal signals with large wavelength (Figures 5a–5c).

[41] In the frequency domain (Figure 7b), the energy at the major tidal constituents, inertial frequency, and diurnal harmonic frequencies, and their enhanced variance in nearby bands are clearly identified. The energy of these motions decays with a factor between σ^{-1} and σ^{-2} at high frequency [e.g., *Ferrari and Wunsch*, 2009]. In the very low frequency band ($\sigma < 2 \times 10^{-2}$ cpd, i.e., $T > 50$ days), the coastal surface current spectra include mesoscale energy to some degree.

4. Summary

[42] High-resolution coastal surface current measurements enabled by the USWC HFR network provide an observational resource to examine the detailed coastal surface variability, including wind coherent and tide coherent (barotropic and baroclinic components) surface currents, poleward signals near the coast, submesoscale eddies, and continuous oceanic scales from submesoscale through mesoscale.

[43] The applied wind regression analysis partitions the components into those forced by local and remote winds and derives a statistical model of wind-driven circulation. The wind skill estimated from local winds ranges from 0.2 to 0.5 and increases from southern California to Oregon and Washington. Moreover, near-inertial motions at the ocean surface, whose amplitudes are coherent with local wind variability, are manifested in the HFR surface currents. The amplitude and phase of the K_1 and M_2 tide coherent surface currents are within the range of those derived from barotropic nearshore and global tidal models. The anomalies from their typical alongshore distribution may be explained with seasonal harmonics of diurnal winds and local baroclinic tidal components, respectively. HFR can complement shoreline tide gauges by expanding the understanding of horizontal variation of tides and by being used as a data source to constrain realistic numerical models.

[44] Poleward propagating alongshore surface currents on the USWC have phase speeds of $O(10)$ and $O(100$ to $300)$ km day^{-1} and time scales of 2 to 3 weeks. Slow mode signals are mainly detected in southern California, which may be a result of reflection and scattering by abrupt coastline curvature near Point Conception preventing them from propagating northward. The poleward signals are possibly interpreted as coastally trapped waves. As an extended use of HFRs, the long-term trend and climate signals propagating up and down the coast, beside surface tides and CTWs, are monitored in near real time.

[45] Submesoscale eddies identified by their flow geometry have diameters of 10 to 60 km, Rossby numbers of 0.1 to 3, and persistence for 2 to 12 days. As a unique observational resource for submesoscale eddies, these will be beneficial to research on turbulent processes and physio-biological interactions, which have mainly depended on theoretical studies and numerical models.

[46] In addition, the HFR surface currents can resolve variability of the surface ocean across scales from submesoscale to mesoscale ($O(1)$ km to $O(1000)$ km). For instance, the wave number spectra of HFR surface currents decay with k^{-2} at high wave number ($L < 100$ km) aligned with spectra reported in the literature of submesoscale processes. Moreover, at low wave number ($L > 100$ km), they are consistent with spectra of cross-track currents estimated from along-track altimeter observations except for energy of waves with long wavelength such as CTWs.

[47] In conclusion, coupled with other ongoing in situ observational programs and satellite remote sensing missions, surface current observations are crucial for monitoring ocean variability continuously in time and space by filling the existing gaps of in situ instruments from offshore to nearshore and can provide timely input and a fundamental scientific resource to the management of coastal waters.

Appendix A: Polarization and Coastal Boundary Effects

[48] In a linearized momentum equation without coastal boundary conditions,

$$\frac{\partial \mathbf{u}}{\partial t} + f_c \times \mathbf{u} + r\mathbf{u} = \nu \frac{\partial^2 \mathbf{u}}{\partial z^2}, \tag{A1}$$

where f_c, r, and ν denote the inertial frequency, frictional coefficient, and kinematic viscosity, respectively ($\mathbf{u} = u + iv$), the power spectrum of currents forced by wind (Ekman model) and by pressure perturbation (internal waves) are

$$S(\sigma) = \frac{1}{|i(\sigma + f_c) + r|}, \tag{A2}$$

$$S(\sigma) = \frac{1}{|i(\sigma + f_c) + r|^2}, \tag{A3}$$

respectively [e.g., *Fofonoff*, 1969; *Gonella*, 1972; *LeBlond and Mysak*, 1978]. For each case, the polarization coefficients without friction ($r = 0$) are A and C in Figure A1. When constant friction was assumed as $0.2f_c$, the polarization coefficients are shown as B and D in Figure A1.

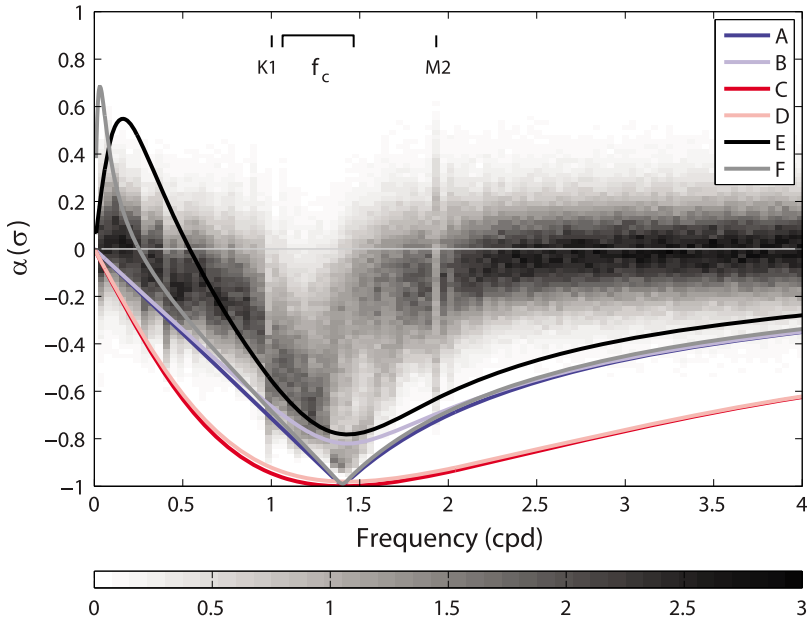

Figure A1. Polarization coefficients of surface currents observed on the USWC and derived from analytic models. Cases A and B are for wind-driven currents (Ekman theory) for $r/f_c = 0$ and $r/f_c = 0.2$, respectively. r and f_c indicate the friction and local inertial frequency ($f_c = 1.40$ cpd). Cases C and D are for pressure-driven currents (internal wave-driven currents) for $r/f_c = 0$ and $r/f_c = 0.2$, respectively. Cases E and F are for currents from the coastal boundary constrained analytic model at $h/\delta_E = 2$ and $h/\delta_E = 10$, respectively (h and δ_E denote the water depth and Ekman depth, and $\nu = 5 \times 10^{-4}$ m^2 s^{-1}).

[49] To examine the coastal boundary effects, a linearized two-dimensional analytic model in the frequency domain is considered.

$$\frac{\partial u}{\partial t} - f_c v = -g\frac{\partial \eta}{\partial x} + \frac{1}{\rho}\frac{\partial \tau_x}{\partial z}, \tag{A4}$$

$$\frac{\partial v}{\partial t} + f_c u = \frac{1}{\rho}\frac{\partial \tau_y}{\partial z}, \tag{A5}$$

where η, τ_x, and τ_y denote sea surface elevation, wind stress in the x and y directions. The model is set up in a straight coast with small sea level slope in the alongshore (y) direction compared to the slope in the cross-shore (x) direction. In addition, in the cross-shore direction, no mass flux, constant eddy viscosity (ν, $\nu = 5 \times 10^{-4}$ m^2 s^{-1}) through the water column, and a no slip boundary condition at the bottom are assumed:

$$\frac{\partial \eta}{\partial y} \ll \frac{\partial \eta}{\partial x} \tag{A6}$$

$$\int u \, dz = 0 \tag{A7}$$

[50] Two cases of bottom topography are considered: a constant depth and linearly increasing depth. The polarization coefficients of currents at the depth of $h = 2\delta_E$ and $h = 10\delta_E$ in the sloping bottom bathymetry are E and F in Figure A1 (h and δ_E denote the water depth and the Ekman depth; $\delta_E = \pi\sqrt{2\nu/f_c}$). In the flat bottom case, the polarization coefficient is nearly the same as F in Figure A1.

[51] **Acknowledgments.** The authors thank the State of California for the funding of the Coastal Ocean Currents Monitoring Program (COCMP), which established statewide current monitoring infrastructure; the National Oceanic and Atmospheric Administration (NOAA) for their continued support of the Integrated Ocean Observing System (IOOS); and, in particular, the leadership of Jack Harlan at NOAA in the establishment of a national HFR program; as well as the sponsorship of the National Science Foundation and Office of Naval Research for early support of the development and use of HFR for ocean research. Data from this report originate from the following universities and research organizations on the USWC: Scripps Institution of Oceanography (SIO) at University of California, San Diego; University of Southern California; Marine Science Institute at University of California, Santa Barbara; California Polytechnic State University; Naval Postgraduate School; Romberg Tiburon Center at San Francisco State University; Humboldt State University; Bodega Marine Laboratory at University of California, Davis; Oregon State University. The three USWC IOOS regional observing systems (SCCOOS, CeNCOOS, and NANOOS) are acknowledged for their continued support and advocacy of HFR current measurements for monitoring the oceans. The coastal wind data and in situ ADCPs were provided by National Data Buoy Center (NDBC). The altimeter products were produced by SSALTO/DUACS and distributed by AVISO with support from CNES. The local mooring data are provided by Orange County Sanitation District (OCSD), Point Loma Ocean Outfall (PLOO), and International Boundary and Water Commission (IBWC). Special thanks to Coastal Ocean Observing and Development Center (CORDC, http://www.cordc.ucsd.edu/) staff and Aurelien Ponte at SIO. The order of coauthors is assigned geographically.

References

Allen, J. S. (1980), Models of wind-driven currents on the continental shelf, *Annu. Rev. Fluid Mech.*, *12*, 389–433.

Barrick, D. E., M. W. Evans, and B. L. Weber (1977), Ocean surface currents mapped by radar, *Science*, *198*(4313), 138–144.

Battisti, D. S., and B. M. Hickey (1984), Application to remote wind-forced coastal trapped wave theory to the Oregon and Washington coasts, *J. Phys. Oceanogr.*, *14*, 887–903.

Beckenbach, E., and L. Washburn (2004), Low-frequency waves in the Santa Barbara Channel observed by high-frequency radar, *J. Geophys. Res.*, *109*, C02010, doi:10.1029/2003JC001999.

Brink, K. H. (1991), Coastal-trapped waves and wind-driven currents over the continental shelf, *Annu. Rev. Fluid Mech.*, *23*, 389–412.

Brink, K. H., and D. C. Chapman (1987), Programs for computing properties of coastal-trapped waves and wind-driven motions over the continental shelf and slope, *Tech. Rep. WHOI-87-24*, Woods Hole Oceanogr. Inst., Woods Hole, Mass.

Brink, K. H., D. C. Chapman, and G. R. Halliwell Jr. (1987), A stochastic model for wind-driven currents over the continental shelf, *J. Geophys. Res.*, *92*, 1783–1797.

Caldeira, R. M. A., P. Marchesiello, N. P. Nezlin, P. M. DiGiacomo, and J. C. McWilliams (2005), Island wakes in the Southern California Bight, *J. Geophys. Res.*, *110*, C11012, doi:10.1029/2004JC002675.

Capet, X., J. C. McWilliams, M. J. Molemaker, and A. F. Shchepetkin (2008), Mesoscale to submesoscale transition in the California Current System. Part I: Flow structure, eddy flux, and observational tests, *J. Phys. Oceanogr.*, *38*, 29–43, doi:10.1175/2007JPO3671.1.

Castelao, R. M., and J. A. Barth (2005), Coastal ocean response to summer upwelling favorable winds in a region of alongshore bottom topography variations off Oregon, *J. Geophys. Res.*, *110*, C10S04, doi:10.1029/2004JC002409.

Chapman, D. C. (1987), Application of wind-forced, long, coastal-trapped wave theory along the California coast, *J. Geophys. Res.*, *92*, 1798–1816.

Chelton, D. B., and R. E. Davis (1982), Monthly mean sea level variability along the West Coast of North America, *J. Phys. Oceanogr.*, *12*, 757–784.

Chelton, D. B., A. W. Bratkovich, R. L. Bernstein, and P. M. Kosro (1988), Poleward flow off central California during the spring and summer of 1981 and 1984, *J. Geophys. Res.*, *93*, 10,604–10,620.

Chelton, D. B., R. A. DeSzoeke, M. G. Schlax, K. E. Naggar, and N. Siwertz (1998), Geophysical variability of the first baroclinic Rossby radius of deformation, *J. Phys. Oceanogr.*, *28*, 433–460.

Crombie, D. D. (1955), Doppler spectrum of sea echo at 13.56 Mc./s, *Nature*, *175*, 681–682.

Davis, R. E., and P. S. Bogden (1989), Variability on the California shelf forced by local and remote winds during the Coastal Ocean Dynamics Experiment, *J. Geophys. Res.*, *94*, 4763–4783.

Dorman, C. E., and C. D. Winant (1995), Buoy observations of the atmosphere along the West Coast of the United States, 1981–1990, *J. Geophys. Res.*, *100*, 16,029–16,044.

Egbert, G. D., and S. Y. Erofeeva (2002), Efficient inverse modeling of barotropic ocean tides, *J. Atmos. Ocean. Technol.*, *19*, 183–204.

Egbert, G., A. Bennett, and M. Foreman (1994), TOPEX/POSEIDON tides estimated using a global inverse model, *J. Geophys. Res.*, *99*, 24,821–24,852.

Ekman, V. W. (1905), On the influence of the Earth's rotation on ocean-currents, *Ark. Mat. Astron. Fys.*, *2*, 1–53.

Emery, B. M., L. Washburn, and J. Harlan (2004), Evaluating radial current measurements from CODAR high-frequency radars with moored current meters, *J. Atmos. Ocean. Technol.*, *21*, 1259–1271.

Erofeeva, S. Y., G. D. Egbert, and P. M. Kosro (2003), Tidal currents on the central Oregon shelf: Models, data, and assimilation, *J. Geophys. Res.*, *108*(C5), 3148, doi:10.1029/2002JC001615.

Ferrari, R., and C. Wunsch (2009), Ocean circulation kinetic energy: Reservoirs, sources, and sinks, *Annu. Rev. Fluid Mech.*, *41*, 253–282, doi:10.1146/annurev.fluid.40.111406.102139.

Fofonoff, N. P. (1969), Spectral characteristics of internal waves in the ocean, *Deep Sea Res. Oceanogr. Abstr.*, *16*, suppl., 58–72.

Gonella, J. (1972), A rotary-component method for analysis in meteorological and oceanographic vector time series, *Deep Sea Res. Oceanogr. Abstr.*, *19*, 833–846.

Gough, M. K., N. Garfield, and E. McPhee-Shaw (2010), An analysis of HF-radar measured surface currents to determine tidal, wind-forced and seasonal circulation in the Gulf of the Farallones, California, United States, *J. Geophys. Res.*, C04019, doi:10.1029/2009JC005644.

Grimshaw, R., and J. S. Allen (1988), Low-frequency baroclinic waves off coastal boundaries, *J. Phys. Oceanogr.*, *18*, 1124–1143.

Halliwell, G. R., Jr., and J. S. Allen (1984), Large-scale sea level response to atmospheric forcing along the West Coast of North America, summer 1973, *J. Phys. Oceanogr.*, *14*, 864–886.

Huyer, A., and P. M. Kosro (1987), Mesoscale surveys over the shelf and slope in the upwelling region near Pt. Arena, California, *J. Geophys. Res.*, *92*, 1655–1681.

Kaplan, D., and J. L. Largier (2006), HF radar-derived origin and destination of surface waters off Bodega Bay, California, *Deep Sea Res., Part II*, *53*(25–26), 2906–2930.

Kaplan, D. M., J. L. Largier, and L. W. Botsford (2005), HF radar observations of surface circulation off Bodega Bay (northern California, USA), *J. Geophys. Res.*, *110*, C10020, doi:10.1029/2005JC002959.

Kaplan, D. M., C. Halle, J. Paduan, and J. L. Largier (2009), Surface currents during anomalous upwelling seasons off central California, *J. Geophys. Res.*, *114*, C12026, doi:10.1029/2009JC005382.

Kim, S. Y. (2010), Observations of submesoscale eddies using high-frequency radar-derived kinematic and dynamic quantities, *Cont. Shelf Res.*, *30*, 1639–1655, doi:10.1016/j.csr.2010.06.011.

Kim, S. Y., E. J. Terrill, and B. D. Cornuelle (2008), Mapping surface currents from HF radar radial velocity measurements using optimal interpolation, *J. Geophys. Res.*, *113*, C10023, doi:10.1029/2007JC004244.

Kim, S. Y., B. D. Cornuelle, and E. J. Terrill (2009a), Anisotropic response of surface currents to the wind in a coastal region, *J. Phys. Oceanogr.*, *39*, 1512–1533, doi:10.1175/2009JPO4013.1.

Kim, S. Y., E. J. Terrill, and B. D. Cornuelle (2009b), Assessing coastal plumes in a region of multiple discharges: The U.S.–Mexico border, *Environ. Sci. Technol.*, *43*(19), 7450–7457, doi:10.1021/es900775p.

Kim, S. Y., B. D. Cornuelle, and E. J. Terrill (2010a), Decomposing observations of high-frequency radar derived surface currents by their forcing mechanisms: Decomposition techniques and spatial structures of decomposed surface currents, *J. Geophys. Res.*, *115*, C12007, doi:10.1029/2010JC006222.

Kim, S. Y., B. D. Cornuelle, and E. J. Terrill (2010b), Decomposing observations of high-frequency radar derived surface currents by their forcing mechanisms: Locally wind-driven surface currents, *J. Geophys. Res.*, *115*, C12046, doi:10.1029/2010JC006223.

Klein, P., and G. Lapeyre (2009), The oceanic vertical pump induced by mesoscale and submesoscale turbulence, *Annu. Rev. Mar. Sci.*, *1*, 351–375, doi:10.1146/annurev.marine.010908.163704.

Kosro, P. M. (2005), On the spatial structure of coastal circulation off Newport, Oregon, during spring and summer 2001 in a region of varying shelf width, *J. Geophys. Res.*, *110*, C10S06, doi:10.1029/2004JC002769.

Largier, J. L., B. A. Magnell, and C. D. Winant (1993), Subtidal circulation over the northern California shelf, *J. Geophys. Res.*, *98*, 18,147–18,179.

LeBlond, P. H., and L. A. Mysak (1978), *Waves in the Ocean*, 602 pp., Elsevier, New York.

Levanon, N. (2000), Lowest GDOP in 2-D scenarios, *IEE Proc. Radar Sonar Navig.*, *147*, 149–155.

Mackas, D. L. (2006), Interdisciplinary oceanography of the western North American continental margin: Vancouver Island to the tip of Baja California, in *The Sea: The Global Coastal Ocean, Interdisciplinary Regional Studies and Syntheses*, vol. 14A, chap. 12, pp. 441–501, Harvard Univ. Press, Cumberland, R. I.

McWilliams, J. C. (1985), Submesoscale, coherent vortices in the ocean, *Rev. Geophys.*, *23*(2), 162–182.

Munk, W. H., and N. Phillips (1968), Coherence and band structure of inertial motion in the sea, *Rev. Geophys.*, *6*(4), 447–472.

Nishimoto, M., and L. Washburn (2002), Patterns of coastal eddy circulation and abundance of pelagic juvenile fish in the Santa Barbara Channel, California, USA, *Mar. Ecol. Prog. Ser.*, *241*, 183–199.

Ocean US (2002), An Integrated and Sustained Ocean Observing System (IOOS) for the United States: Design and Implementation, *Tech. rep.*, Arlington, Va.

Ohlmann, C., P. White, L. Washburn, E. Terrill, B. Emery, and M. Otero (2007), Interpretation of coastal HF radar-derived surface currents with high-resolution drifter data, *J. Atmos. Ocean. Technol.*, *24*, 666–680.

Overland, J. E., and C. H. Pease (1988), Modeling ice dynamics of coastal seas, *J. Geophys. Res.*, *93*, 15,619–15,637.

Paduan, J. D., and L. K. Rosenfeld (1996), Remotely sensed surface currents in Monterey Bay from shore-based HF radar (Coastal Ocean Dynamics Application Radar), *J. Geophys. Res.*, *101*, 20,669–20,686.

Pawlowicz, R., B. Beardsley, and S. Lentz (2002), Classic tidal harmonic analysis including error estimates in MATLAB using T_TIDE, *Comp. Geosci.*, *28*, 929–937.

Priestley, M. B. (1981), *Spectral Analysis and Time Series*, 890 pp., Academic, London.

Ramp, S. R., L. K. Rosenfeld, T. D. Tisch, and M. R. Hicks (1997), Moored observations of the current and temperature structure over the continental shelf off central California: 1. A basic description of the variability, *J. Geophys. Res.*, *102*, 22,877–22,902.

Ray, R. D., and G. D. Egbert (2004), The global S_1 tide, *J. Phys. Oceanogr.*, *34*, 1922–1935.

Rosenfeld, L. K., and R. C. Beardsley (1987), Barotropic semidiurnal tidal currents off Northern California during the Coastal Ocean Dynamics Experiment (CODE), *J. Geophys. Res.*, *92*, 1721–1732.

Rosenfeld, L., I. Shulman, M. Cook, J. Paduan, and L. Shulman (2009), Methodology for a regional tidal model evaluation, with application to

central California, *Deep Sea Res., Part II*, *56*, 199–218, doi:10.1016/j.dsr2.2008.08.007.

Schneider, T. (2001), Analysis of incomplete climate data: Estimation of mean values and covariance matrices and imputation of missing values, *J. Clim.*, *14*, 853–871.

Shay, L. K., H. C. Graber, D. B. Ross, and R. D. Chapman (1995), Mesoscale ocean surface current structure detected by high-frequency radar, *J. Atmos. Ocean. Technol.*, *12*, 881–900.

Spargo, E. A., J. J. Westerink, J. Richard, A. Luettich, and D. J. Mark (2004), ENPAC 2003: A tidal constituent database for eastern North Pacific Ocean, *Tech. Rep. ERDC/CHL TR-04-12*, Coastal and Hydraul. Lab., U.S. Army Corps of Eng., Washington, D. C.

Spillane, M. C., D. B. Enfield, and J. S. Allen (1987), Intraseasonal oscillations in sea level along the West Coast of the Americas, *J. Phys. Oceanogr.*, *17*, 313–325.

Stammer, D. (1997), Global characteristics of ocean variablity estimated from regional TOPEX/POSEIDON altimeter measurements, *J. Phys. Oceanogr.*, *27*, 1743–1769.

Stewart, R. H., and J. W. Joy (1974), HF radio measurements of surface currents, *Deep Sea Res. Oceanogr. Abstr.*, *21*, 1039–1049.

Strub, P. T., and C. James (2000), Altimeter-derived variability of surface velocities in the California Current System: 2. Seasonal circulation and eddy statistics, *Deep Sea Res., Part II*, *47*, 831–870.

Strub, P. T., J. S. Allen, A. Huyer, R. L. Smith, and R. C. Beardsley (1987), Seasonal cycles of currents, temperatures, winds, and sea level over the northeast Pacific continental shelf: 35°N to 48°N, *J. Geophys. Res.*, *92*, 1507–1526.

Strub, P. T., P. Kosro, A. Huyer, and CTZ Collaborators (1991), The nature of the cold filaments in the California Current System, *J. Geophys. Res.*, *96*, 14,743–14,768.

Terrill, E. J., et al. (2006), Data management and real-time distribution in the HF-radar national network, in *OCEANS 2006*, pp. 1–6, Inst. Electr. Electr. Eng., Boston, doi:10.1109/OCEANS.2006.306883.

Ullman, D. S., J. O'Donnell, J. Kohut, T. Fake, and A. Allen (2006), Trajectory prediction using HF radar surface currents: Monte Carlo simulations of prediction uncertainties, *J. Geophys. Res.*, C12005, doi:10.1029/2006JC003715.

von Storch, H., and F. Zwiers (1999), *Statistical Analysis in Climate Research*, 484 pp., Cambridge Univ. Press, New York.

Wilkin, J. L., and D. C. Chapman (1990), Scattering of coastal-trapped waves by irregularities in coastline and topography, *J. Phys. Oceanogr.*, *20*, 396–421.

Wolanski, E., J. Imberger, and M. L. Heron (1984), Island wakes in shallow coastal waters, *J. Geophys. Res.*, *89*, 10,553–10,569.

B. D. Cornuelle, S. Y. Kim, and E. J. Terrill, Scripps Institution of Oceanography, 9500 Gilman Dr., La Jolla, CA 92093, USA. (syongkim@mpl.ucsd.edu)

G. Crawford, Faculty of Science and Technology, Vancouver Island University, 900 Fifth St., Nanaimo, BC V9T 5S5, Canada.

N. Garfield, Geosciences Department, San Francisco State University, 3152 Paradise Dr., Tiburon, CA 94920, USA.

B. Jones, Department of Biological Sciences, University of Southern California, 3616 Trousdale Pkwy., AHF B-30, Los Angeles, CA 90089, USA.

P. M. Kosro, College of Oceanic and Atmospheric Sciences, Oregon State University, 104 COAS Administration Bldg., Corvallis, OR 97331, USA.

J. L. Largier, Bodega Marine Laboratory, University of California, Davis, PO Box 247, Bodega Bay, CA 94923, USA.

M. A. Moline, Biological Sciences Department, California Polytechnic State University, San Luis Obispo, CA 93407, USA.

J. D. Paduan, Department of Oceanography, Graduate School of Engineering and Applied Sciences, Naval Postgraduate School, Code OC/Pd, Monterey, CA 93943, USA.

L. Washburn, Institute for Computational Earth System Science, Department of Geography, University of California, Santa Barbara, CA 93106, USA.